minerals

MDPI

Article

Identification and Evolution of Different Genetic Types of Deep Karst Caves Controlled by Faults—A Case Study in Huanjiang Sag, Guangxi Province, South China

Yong Dan [1], Hongqi Dong [1,*], Bin Liang [1], Guoquan Nie [1], Xiuquan Hu [2], Shaocong Ji [1] and Kai Han [1]

[1] Institute of Karst Geology, Chinese Academy of Geological Sciences, Guilin 541004, China; danyong@karst.ac.cn (Y.D.); liangbin@mail.cgs.gov.cn (B.L.); nieguoquan@mail.cgs.gov.cn (G.N.); jishaocong@mail.cgs.gov.cn (S.J.); hankai@karst.ac.cn (K.H.)

[2] College of Energy, Chengdu University of Technology, Chengdu 610059, China; huxiuquan15@cdut.edu.cn

* Correspondence: donghongqi@mail.cgs.gov.cn; Tel.: +86-188-783-31719

Abstract: In recent years, it has become more and more common to drill deep karst caves as a part of deep shale gas resource exploration and engineering construction in South China. However, the amount of research on the genesis and development mechanism of deep karst caves is relatively low. Based on drilling core karst morphology analysis and two-dimensional (2D) seismic and wide-field geophysical exploration methods, it is revealed that the deep karst in the Huanjiang area is mainly composed of net cracks, holes expanding along cracks and dolomite honeycomb pores, and that large karst caves are also developed, which are related to NW-trending faults. The deep karst is developed in the hanging wall of the fault, with a width of 500 m and a height of 1500 m, and a linear distribution along NW faults in the region. Based on Th-U dating, inclusion testing and rare earth elements from cave fillings, it is revealed that the development of deep karst space is related to two deep karst genetic types: The first is the hypogene hydrothermal karst, which developed in the Yanshanian period and is related to regional magmatism. The second is the groundwater deep circulation karst, mainly developed after the Himalayan period, which is related to the deep circulation of meteoric water. The genesis of deep karst space is the result of multi-stage karst superposition and is mainly controlled by faults. It is difficult to determine the specific time points of these two types of deep karst transformation, but according to regional tectonic evolution, we speculate that the Yunnan-Guizhou Plateau has been uplifted since the Himalayan period (>3.54 Ma), and the Carboniferous carbonate rocks and early faults in the Huanjiang area have been exposed, leading to the change and evolution of deep karst. Through comprehensive analysis, a fault-controlled hypogene hydrothermal karst pattern and a meteoric water deep karst pattern are established. The genetic pattern of deep karst provides theoretical support for predicting this kind of karst in southern China and for avoiding drilling deep karst caves as a part of resource exploitation.

Keywords: deep karst; hypogene karst; hydrothermal karst; karst pattern

check for updates

Citation: Dan, Y.; Dong, H.; Liang, B.; Nie, G.; Hu, X.; Ji, S.; Han, K. Identification and Evolution of Different Genetic Types of Deep Karst Caves Controlled by Faults—A Case Study in Huanjiang Sag, Guangxi Province, South China. *Minerals* **2022**, *12*, 405. https://doi.org/10.3390/min12040405

Academic Editor: Stanisław Mazur

Received: 22 February 2022
Accepted: 21 March 2022
Published: 25 March 2022

Publisher's Note: MDPI stays neutral with regard to jurisdictional claims in published maps and institutional affiliations.

Copyright: © 2022 by the authors. Licensee MDPI, Basel, Switzerland. This article is an open access article distributed under the terms and conditions of the Creative Commons Attribution (CC BY) license (https://creativecommons.org/licenses/by/4.0/).

1. Introduction

In the 20th century, many karst studies concerned with shallow, hydrogeologically unconfined settings were conducted. The main characteristic of this karst is recharge by meteoric water, with the water moving from the top to the bottom of the recharge area to form karst caves, which Palmer [1] classified as epigenic karst. Since the 1960s, it has gradually been recognized that hot fluid moves upward from the deep to form dissolution caves [2–7]. In the 1970s and the 1980s, the dissolution of sulfuric acid produced by the oxidation of deep fluid with high H_2S was also recognized [8–10]. At the end of the 20th century, the concepts of hypogene karst and hypogene speleogenesis were formally put forward [1,6,9], and Palmer's research results resulted in a karst classification [1,11]. A large number of hypogene karst caves have been discovered around the world in the

last 20 years (e.g., in Eastern Europe, western Ukraine, central Italy, the Middle East, New Mexico, Tennessee, and Australia). Phenomena that could not be explained with reference to epigenic karst in the past are now well explained with reference to hypogene karst [12–16]. Therefore, it has to be admitted that two different types of karst, hypogene karst and epigenic meteoric water karst, are equally important.

Karst mainly emphasizes spatial division in actual production. It is generally believed that the karsts located in the deep slow flow zone below the local drainage base level (usually the local river) are all classified as deep karst [17], and that the karsts above the local drainage base level belong to shallow karst. Deep karstification is not controlled by the local drainage base level. Recently, with the implementation of large hydraulic engineering, hypogene geothermal resource exploitation and deep oil–gas resource exploitation in China, many deep karst caves have been found in drilling and engineering processes [18–22], which has attracted attention. For the genesis of these deep karst caves, based on a small number of well core tests and the analysis of the basic conditions for karst development, many Chinese scholars have proposed the genetic explanations of valley-type deep karst, syncline basin-type deep karst [17], deep karst controlled by compression-torsion structure [23], deep hydrothermal karst and deep organic acid karst [21,24,25]. Dong et al. [16] established the deep circulation karst pattern of groundwater in Huanjiang based on a comparative analysis of isotopes between deep karst cave groundwater and regional spring groundwater. Compared to near-surface shallow karst, which people can enter via karst caves to carry out measurements and sampling, how do we study how different fluids control the development of deep karst? And how can a single genetic mechanism explain the causes of deep karst? Moreover, it is difficult to directly obtain geological evidence for the study of the causes of deep karst. Therefore, there has not been a lot of exploration and research on the genesis and the development mechanism of deep karst [26].

During shale gas drilling in Huanjiang Sag, Guangxi, China, from 2016 to 2018, deep karst caves were found in the process of drilling through carbonate rock in order to explore shale gas in the lower part of the rock. More than 20 karst caves were found in four wells, distributed 70–1200 m below ground, and the maximum cave height was 20 m. Thanks to shale gas-well coring in four wells and a lot of geophysical work having been done in shale gas exploration, as well as the long-term monitoring of groundwater in these deep karst carried out by Dong et al. [16], the above works provide a lot of basic data and geological evidence for the study of the genesis of deep karst. Based on the above data, this paper further studies the karst morphology of drilling cores, and the through-well geophysics and geochemical composition of karst cave fillings. Combined with the previous comprehensive analysis of regional deep karst groundwater, the stages and genetic types of deep karst are analyzed, and the main controlling factors for its formation are discussed. The study of deep karst in Huanjiang can serve as a reference for understanding the process and the genesis mechanism of deep karst in other regions around the world, and has great significance for enriching the geological theory of karst. It provides theoretical support for predicting the karst cave distribution in the vast south of China and for avoiding drilling deep karst caves in the course of resource exploitation.

2. Geologic Setting

Huanjiang Sag is located in the northwest of Guangxi province in southern China (Figure 1) and covers 2000 km^2, much of which is covered by Carboniferous rock formations, with only a sporadic occurrence of Permian and Triassic rock formations. A Devonian rock formation is exposed around the sag, and the boundaries of the sag are the North–Northeast and North–West striking faults. After the Carboniferous deposition, the Hercynian movement in this area was in the form of up-and-down movement, while the Indosinian movement was a common and intense fold movement, which ended the marine deposition process in Huanjiang Sag and replaced it with continental deposition. Later, the Yanshan Movement was dominated by the development of NW-striking faults, accompa-

nied by the intrusion of magma. After the Himalayan Movement, folded structures in this area formed mountains. Affected by multi-stage tectonics, ruptures and folds developed in Huanjiang Sag, with more developing in the high angle fault zone. Most of the faults are normal faults, while a few are reverse faults. The general strike of the structure line is in the NNE–SSW direction, with dip angles of 5~20° of strata, and angles of more than 20° only in the vicinity of large fault zones. Trapped syncline and anticline developed in the Huanjiang Sag anticline axis generally exposes silicalite and marlstone of the middle–upper Devonian. The syncline mostly exposes upper Carboniferous, but also lower Permian in the fold axis zone. The dip angle of strata in fold limbs is generally 10–20°, and locally it is greater than 20° [27–29].

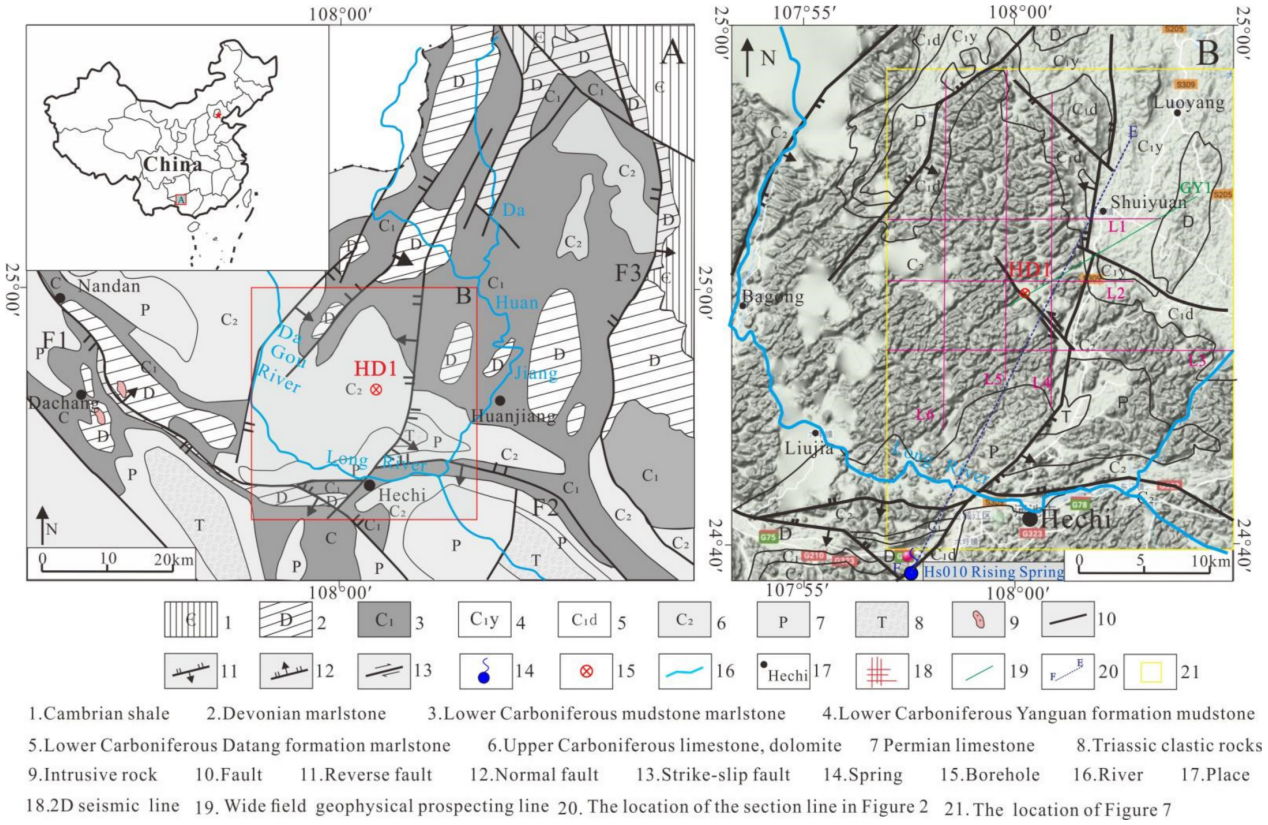


Figure 1. Tectonic location of the Huanjiang area. (**A**) Regional geological map of Huanjiang Sag, Guangxi. (**B**) Karst geomorphic map of Huanjiang Sag, Guangxi. Note: Figure 1A is from a geological survey of Guangxi, 1971 [28]; (**B**) is from Google Earth.

The soluble carbonate rocks in the area are Carboniferous-Permian platform facies carbonate rocks with large area outcropping; however, karstification of marlstone and silicalite in Devonian and clastic rocks in Triassic is not found. The main karst strata are the Datang formation of Lower Carboniferous, the Dapu, Huanglong, and Maping formations of Upper Carboniferous, and the Qixia, Maokou, and Heshan formations of Permian, with an accumulative thickness of thousands of meters (Figure 2). Except for the Dapu formation, which is a set of fine–medium dolomites and lime–dolostone, the formations are pure limestone, which belongs to the continuous formation of mega-thick carbonate rocks (>2000 m) with strong solubility [16]. The argillaceous content in the lower part of Lower Carboniferous increases and gradually transitions to the large shale of the Yanguan formation of the Lower Carboniferous, which is the bottom boundary of karstification [16].

The study area has a subtropical monsoon climate, with an annual average temperature of 19.9 °C. Rainfall is concentrated mostly in the rainy season (June–September), which accounts for more than 75% of the total annual rainfall; annual average rainfall is 1389.1–

1750.3 mm. In addition, Huanjiang syncline is located mainly on the southern slope of the Yunnan-Guizhou Plateau [16]. The terrain is high in the north and low in the south (Figures 1B and 2). The surface drainage flows from north to south and turns to the east near Hechi, affected by the east–west striking faults [30,31]. With abundant precipitation, appropriate temperature and a large set of carbonate rocks, coupled with certain hydrodynamic conditions, the surface karst develops strongly, forming the typical peak-karst landform in the area.

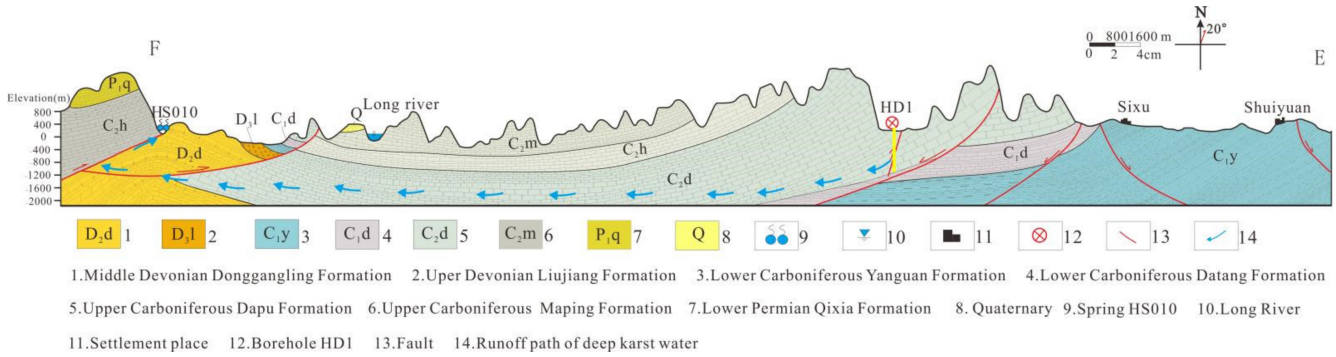


Figure 2. Sectional view of actual geological map of deep karst in Huanjiang sag [16]. (The deep karst groundwater of HD1 well in the northern part of the syncline recharges the karst spring HS010 in the southern part of the syncline through the fracture zone). The plane position of this drawing is shown in Figure 1B.

The Huandi 1 wells (HD1) are located in the syncline basin of the Huanjiang sag with a sea level elevation of 200 m. Four wells (HD1-1, HD1-2, HD1-3, HD1-4) are located within 100 m, as the drill was moved three times due to detection of deep karst caves in the drilling process (The relative positions of the four wells are shown in Supplementary Material Figure S1). The depth of the four wells are 864 m, 887 m, 474 m, and 1971 m, respectively. The main strata drilled from top to bottom are dolomite and dolomitic limestone of the Dapu Formation of Upper Carboniferous (0~600 m), and limestone of the Datang Formation of Carboniferous (below 600 m). These four wells drilled through more than 20 deep karst caves in carbonate strata, with a maximum height of more than 20 m, and most of them were below the lowest drainage base level (current sea level), belonging to deep karst caves. Due to the full well core and abundant through-well geophysical data obtained from the four wells, this has developed to be good material for deep karst research.

3. Methods and Test

As a benefit of shale gas exploration in the region, in addition to the core of the whole well section obtained from the four wells, six two-dimensional seismic profiles were implemented near the wells, with a total of 110 km, and a wide-field electromagnetic method profile was implemented for 17 km. This provides a good research foundation for comprehensively identifying the corrosion morphology and the distribution characteristics of deep caves, and for directly obtaining genetic and geochemical evidence of deep caves.

3.1. Karst Morphological Analysis Method for Deep Karst

A solutional cave is a macroscopic space in a rock created and shaped by moving aggressive fluids, and morphology is the fundamental attribute of the cave that reflects its origin and evolution. Thus, morphogenetic analysis of the caves aimed to reconstruct the geological controls of the speleogenesis and the parameters of speleogenetic agents [5,32].

Karst morphology studies are based on field observations as well as on physical and numerical patterns [6,7,11,32,33]. For surface or near-surface caves, people can directly go in to measure, observe and sample, but it is more difficult to identify and analyze the morphology of deep karst fractures and caves, which can only be identified through

drilling and geophysical exploration [26]. Using drilling cores is the most direct method, and drilling engineering anomalies, such as leakage or emptying phenomena are also an important means of judgment [34]. The karst morphology observation, measurement and classification statistics were carried out on the cores of the whole section of the four wells. Combined with the abnormal statistics of drilling engineering, the classification and identification were carried out according to solution pores and cavities space morphology, dissolution morphology related to structural fractures, filling morphology in dissolution space. Subsequently, the identification results of different types of karst morphology are marked on the drilling histogram, showing the vertical distribution of karst. In addition, through a comparative study between different drillings, the spatial distribution of caves can be understood horizontally.

3.2. Geophysical Exploration and Identification Method

Only the karst morphology near the well can be identified by drilling cores. However, combining the results of drilling identification with the geophysics of passing wells can further identify the spatial morphology of deep karst in the region, as well as its relationship with structure and stratigraphy. These methods are commonly used in paleokarst reservoir research [34].

3.2.1. Two-Dimensional Seismic Interpretation and Analysis Method

Six two-dimensional seismic profiles in the work area were collected (Figure 1B). The seismic acquisition parameters are: instrument model = 428 XL, Sercel company, Carquefou, French; detector type = 30 DX − 10 Hz; number of detectors = 2 strings (20 in total); observation system = 2L1S wide-line observation; number of receiving channels = 480 × 2 = 960 channels; track spacing = 20 m; receiving line distance = 40 m; coverage times = 240 (L2 line)/160 (other lines); shot distance = 40 m (L2 line)/60 m (other lines).

The strata and faults were interpreted by using 'Discovery 2015′ software, LandMark company, Aventura, FL, USA (before and after seismic profiles are explained in Supplementary Material Figures S4–S9). Seismic wave frequency attenuation gradient technology was used for plane karst fracture and cave prediction [35]. When seismic waves propagate underground, the high-frequency components attenuate faster, and the attenuation of seismic waves is proportional to the frequency [35]. When there are fractures and caves in the formation or the reservoir is rich in fluid media, the absorption effect of the formation will be stronger. It is stronger, the greater the attenuation gradient. Some scholars have used this method to identify carbonate cave reservoirs in the Tahe Oilfield, China, and the application effect was good [36]. 'EPoffice EPS+' software, LandOcean energy services compangy, Beijing, China, was used to identify the fractures and caves. A large attenuation gradient indicates fractures and caves, which are represented with red color in the plan figure.

3.2.2. Wide-Field Electromagnetic Method

The wide-field electromagnetic method is a frequency domain electromagnetic sounding method of artificial source, and its detection method and principle refer to [37], who detected geoelectric information at different depths by sending and receiving signals of different frequencies. This time, the maximum emission current of low frequency was 38 A, the minimum emission current of high frequency was 2 A, and the transmitting voltage was 960 V. The wide-field geophysical line passed through well HD1, the azimuth of the line is 61°, the length is 17 km, the point distance is 100 m, and 163 measuring points were arranged. The number of frequencies collected by a single measuring data point is 68, and the collection frequency range is ~0.0117–8192 Hz.

The method can identify strata according to formation resistivity, and effectively identify the geological bodies with obvious differences in underground resistivity, such as a low resistivity water-bearing karst fracture-cave body in the high resistivity of carbonate rocks. The resistance data are plotted using 'sufer10.0' software, Golden software Inc.,

Golden, CO, USA, blue represents the low-resistance geological body, and red represents the high-resistance geological body

3.3. Geochemical Analysis Method of Karst Fillings

Through the test and analysis of fracture-cavity fillings, the formation environment of fillings can be directly reflected, and the fluid properties of karstification at different times can be analyzed to determine the causes of karstification.

3.3.1. Determination Method of Deep Karst Cave Filling Period

To obtain the filling period of the cave, C^{14} and sporopollen analyses of mud fillings collected from a depth of 429 m in the karst caves were performed. The results of the C^{14} test showed that the age of the mud fillings exceeded the detection range of C^{14}, estimated to be >40,000 years. Regrettably, in two batches of mud fillings sent to the Nanjing Institute of Palaeobiology for sporopollen analysis, no sporopollen was found. Previous research [16] has claimed that the deep cave water of HD1 actually received meteoric water recharge. Since it is affected by meteoric water, the Th-U dating method for near-surface caves established by Shen et al. [38] and Cheng et al. [39] can be used. Therefore, the key to dating is to extract calcite affected by meteoric water. After selection, we took an earthy yellow medium-fine crystal calcite at 421 m of the cave wall, and excluded clean calcite. Since the selected calcite is the outermost calcite of the cave wall, its age can reflect the relatively recent development of the cave.

Th-U dating was completed in the Isotope Laboratory of Xi'an Jiaotong University. The chemical process for Uranium and Thorium separation was performed according to Shen et al. [38], and the test instrument was a Thermo Neptune multi-receiver plasma mass spectrometer. The instrument test and the age calculation were based on Cheng et al. [39].

3.3.2. Analysis of Rare Earth Elements in Mud Filling of Karst Cave

Argillaceous materials were mainly collected from the reddish-brown mud fillings at 47 m and 429 m of HD1-4 well caves and brick-red iron-infected calcite at 1220.4 m. All samples were crushed and powdered down to a grain-size smaller than 200 mesh for geochemical analyses. A total of 500 mg of powder was obtained for each sample. Approximately 200 mg of powdered samples were analyzed for rare earth elements. For rare earth elements, samples were cleaned in ultra-pure water before dissolution in 2 mL of 15 N double-distilled HNO_3. Solutions were then spiked with 10 ppb of internal standards for NexION300D ICP-MS (ELAN DRC-e) analyses, Perkin-elmer company, Waltham, MA, USA, with an analytical precision better than 5%. The experimental procedures have been described in other publications (e.g., Nothdurft et al. [40]).

3.3.3. Fluid Inclusion Analysis of Cave Calcite and Dolomite

The selected samples are from the cave calcite and dolomite. The homogenization temperature and freezing point temperature data involved were completed in the Karst Geological Resources Environmental Monitoring Center, Ministry of Natural Resources. The instrument used was the cold and heat table of Linkam and the model number was THMS600, Linkam companhy, Britain. The salinity (wt.% NaCl equivalent) of aqueous inclusions was calculated based on Tm values.

4. Identification Results of Deep Karst Morphology in the Well

There are two kinds of typical corrosion characteristics in cores, including dissolution space morphology and dissolution filling morphology. Dissolution space morphology can be divided into dissolution pores and cracks. Dissolution filling morphology includes mechanical filling morphology and chemical filling morphology.

4.1. Dissolution Pores and Cavities Space Morphology

Through the observation of the core, the dissolution pores and cavities can be divided into pinholes, holes and caves (Dissolution photos and related descriptions are shown in Supplementary Material Figure S2). Needle dissolution pores are dissolution pores less than 2 mm in diameter, densely distributed and unfilled. Needle holes are distributed in four wells at each depth. The diameter of honeycomb dissolved pores is larger than that of pinholes, roughly 2–20 mm, with a dense distribution and a shape similar to honeycomb. The development of honeycomb dissolved pores in the rock reflects that it has good porosity and permeability. The development of honeycomb pores may be related to the further corrosion and expansion of needle-like pores, and unfilled or semi-filled pores are the main types. The diameter of the cavity is about 2–40 cm, and the dissolution space is larger. It is generally formed by further dissolution expansion along cracks or honeycomb holes. This type of hole is developed in only a few strong karst sections in HD1-4. For example, there is a 3 m-strong dissolution section developed at 232 m, and pores are developed which are formed by vertical fracture expansion and dissolution, and filled with earthen-yellow clay. In flesh-like dissolution, cracks in the rock network of the cave wall develop and are dissolved into a melon-like shape by strong dissolution, and become earthy-yellow with the participation of meteoric water, indicating that the cave wall is in long-term contact with groundwater, resulting in strong dissolution. For a total of 23 times in 4 wells, large caves were emptied during drilling construction, and the maximum cave height was 25.8 m. There were mud fillings in the cave and the dissolution joints, as well as expansion holes and gravel formed by karst in the rock center (Table 1).

Table 1. Statistical table of emptying sections of the four drills of HD1 Well.

Number	Well Number	Emptying Section	Cave Height (m)	Number	Well Number	Emptying Section	Cave Height (m)
1	HD1-1	766.00–766.20	0.2	13	HD1-4	417.10–418.90	1.8
2		842.90–864.16	21.26	14		421.75–425.29	3.54
3	HD1-2	861.58–887.38	25.8	15		426.29–429.00	2.71
4	HD1-3	172.50–174.45	1.95	16		429.63–432.10	2.47
5		176.75–177.59	0.85	17		432.70–435.11	2.41
6		440.49–442.64	2.15	18		448.37–451.01	2.64
7		445.07–449.99	4.92	19		451.45–453.05	1.6
8		453.68–474.59	20.91	20		454.70–455.80	1.1
9	HD1-4	46.96–49.56	2.6	21		1126.90–1129.30	2.4
10		49.96–54.16	4.2	22		1158.00–1160.30	2.3
11		73.26–76.26	3	23		1206.00–1208.40	2.4
12		76.96–78.16	1.2				

4.2. Dissolution Morphology Related to Structural Fractures

In addition to the general dissolution morphology in the core of well HD1, there were many instances of broken dissolution morphology related to tectonic movement. Their categories are described in the following.

Rock network cracking: Rock fragmentation caused by tectonic movement, forming multiple sets of microcracks (Figure 3a,b), expansion or filling along cracks (Figure 3b,f). Network cracks are formed in the core, or dissolution pores are formed along the cracks. Patchy rock: tectonic movement causes the rock to break up, forming large fractures that diffuse along the fractures and fill with white calcite or dolomite to form white patches (Figure 3c,d), which are the result of a combination of tectonics and corrosion. Rock brecciation: Rock is extremely broken due to tectonic movement, forming breccia. There is fluid activity between the breccias, filled with white dolomite or calcite (Figure 3c–e). Growth of fault calcite veins: intense tectonic movement causes the rock to dislocate or break, with no bedrock in the core, all later filled with white calcite (Figure 3h).



Figure 3. Dissolution morphology related to fractures in deep karst space of wells HD1-4. (**a**) Micro network cracking, 464 m; (**b**) Micro network cracking, 415 m; (**c**–**e**) Further dissolution of structural breccias and cracks, improving the gravel roundness, and dissolved cracks and holes filled with white dolomite, 444–448 m; (**f**,**g**) Structural network cracking zone, semi-fully filled by white calcite and tending to maculosus in 1718–1721 m; (**h**) Structural calcite vein, 6 m long and developing in fault core, 1454–1460 m.

4.3. Filling Morphology in Dissolution Space

Chemical deposits and mud fillings are visible in the cores. Mud fillings of karst caves can be seen in the depth of 75 m, 230 m, and 426–448 m in well HD1-4 (Figure 4a, Supplementary Material Figure S2), and a large number of earthy yellow mud can be seen at.



Figure 4. Characteristics of fillings in dissolution space. (**a**) Mud filling in caves, 46–46.46 m, HD1-4; (**b**) Caves filled with mud, 863–881 m, HD1-1; (**c**) Earthy yellow fine crystalline calcite growing in the cave wall, 421.05 m, HD1-4; (**d**) The cave calcite fillings infected by brick-red iron in the cave (1131–1138 m) of the HD1-4 well were speculated to be formed after the formation of white calcite dissolved by meteoric water in the later stage, and iron was oxidized to red. (**e**) Cave calcite fillings infected by brick-red iron in the cave, 1218 m; (**f**) Calcite of better crystal form growing in the hole, partly dyed brick-red, 1088 m, HD1-4.

881–885 m of well HD1-1(Figure 4b). Chemical deposits in dissolution space mainly include clean, coarse-grained calcite (Figures 3f–h and 4f), fine-grained calcite grown on

the wall of the cave, earthy yellow calcite (Figure 4c) and calcite infected with brick-red iron (Figure 4d,e), as well as white dolomite deposits (Figure 3c–e).

The identified dissolution pores, cavities, fractures and the filling morphology were marked on the drilling histogram (Figure 5).

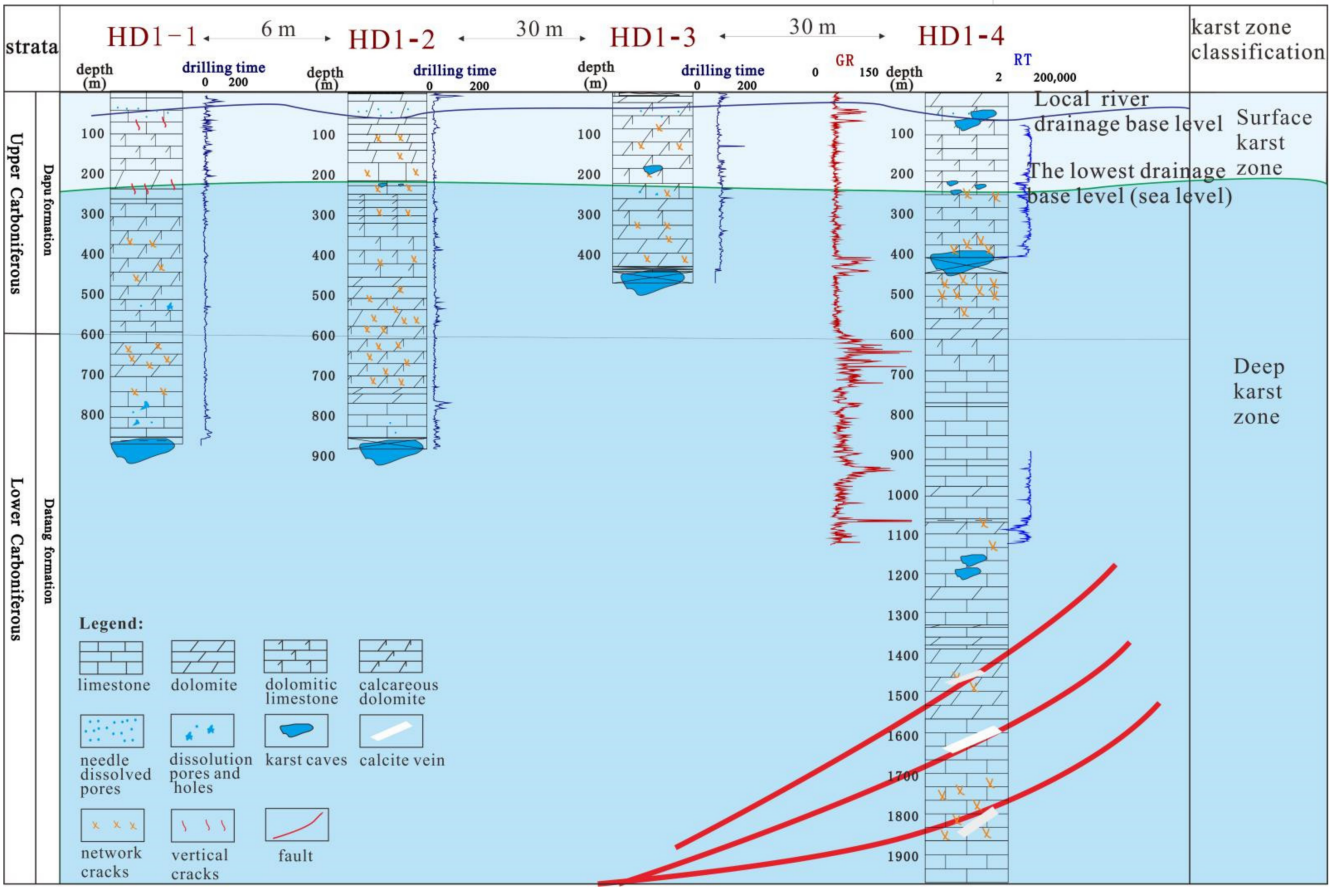


Figure 5. Comparison of deep karst caves developed in drills in Huanjiang sag. The locations of the four wells are shown in Supplementary Material Figure S1.

5. Spatial Distribution of Deep Karst

5.1. Combined Characteristics of Deep Karst Development

The drilling site is located at an altitude of about 200 m, so 200 m above the well is defined as the surface karst that may be affected by the discharge datum, and below 200 m as the deep karst zone (Figure 5). According to the analysis of karst morphology, the deep karst of the four wells is mainly composed of network cracks, solution-expanding holes along the cracks, and dolomite honeycomb holes, and large karst caves are also developed. Through the comparative analysis of four wells, it was found that the development of deep karst caves has the characteristics of multi-layer superposition. According to depth, this can be divided into a 230 m corrosion cavity section, a 450 m fracture cavity section, an 850 m fracture cavity section and a 1200 m fracture cavity section. Additionally, a large number of network cracks and expansion karst cracks develop near the caves (Figure 4). According to the comparison of the filling characteristics of each section, it was found that the depth of 0–1200 m in the deep dissolution space is strongly corroded, and the overall filling degree of the dissolution space is mainly un-semi-filling. It can be seen as a two-stage filling, filled with calcite in the first stage and refilled with mud in the second stage. Through core observation, it was found that the earthy yellow mud fillings decrease in number after the 850 m karst cave section in the deep karst space, and that calcite increases below. However, calcite infected by brick red could be found in caves at depths of 1218 m

(Figure 4e). Brick-red material represents iron oxidation, indicating that surface water can infiltrate to 1218 m, yielding dissolution and oxidation. There are three thick calcite veins below 1400 m (Figures 3h and 5), and the single layer thickness reaches 6 m. The cracks are developed in the upper and lower bedrock, which is speculated to be the core of the fault. Brick red represents iron oxidation, indicating that surface water can penetrate all the way to 1218 m for dissolution and oxidation.

5.2. Geophysical Identification and Distribution Characteristics of Deep Karst

The deep karst space was further characterised by geophysical methods. The two-dimensional seismic section L2 crossing the well (Figures 6 and 7) shows that the seismic facies near the drilling location are discontinuous and that there is a fault. Further identification by the wide-field electromagnetic method shows that there is an ellipse with low resistance (light blue), about 500 m in the east-west direction (vertical fault strike direction), and up to 1500 m in depth near the drilling location with relatively high resistance (red). This depth is basically consistent with the unfilled deep fracture-cavity space developed in the core observation in chapter 5.1 and has good correspondence. Further, seismic wave frequency attenuation gradient technology was used to predict the deep karst plane. It was found that the drilling location of HD1 is represented by an obvious bright red spot (Figure 7, Supplementary Material Figure S5), and that the red bright spot line up in the region. It is speculated that the development range of deep karst in Huanjiang sag is wide and that the whole distribution is linear along the fault (Figure 7).

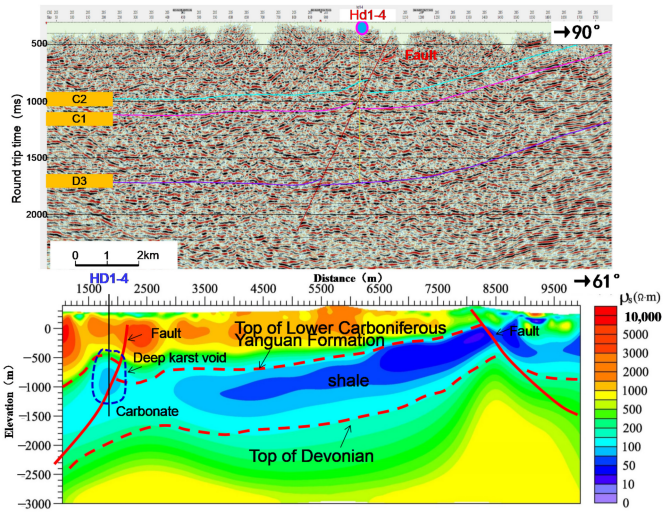


Figure 6. Geophysical identification of faults and caves in Huanjiang Sag. Above is the L2 2D Seismic Geological Interpretation Profile; the seismic section near Well HD 1-4 are discontinuous, indicating a presence of a reverse fault there in combination with drilling cores; below is the GY-1 wide-field electromagnetic geological interpretation section; in the high-resistivity strata, low-resistivity geological bodies are developed near HD1-4, which was confirmed to be a karst space in combination with drilling cores. Note: The plane locations of the geophysical L2 and GY-1 lines are shown in Figure 1B, and the uninterpreted seismic profile of L2 is shown in Supplementary Material Figure S5. C2 = Top of Lower Carboniferous Yanguan Formation, C1 = Top of Devonian, D3 = Top of Middle Devonian.

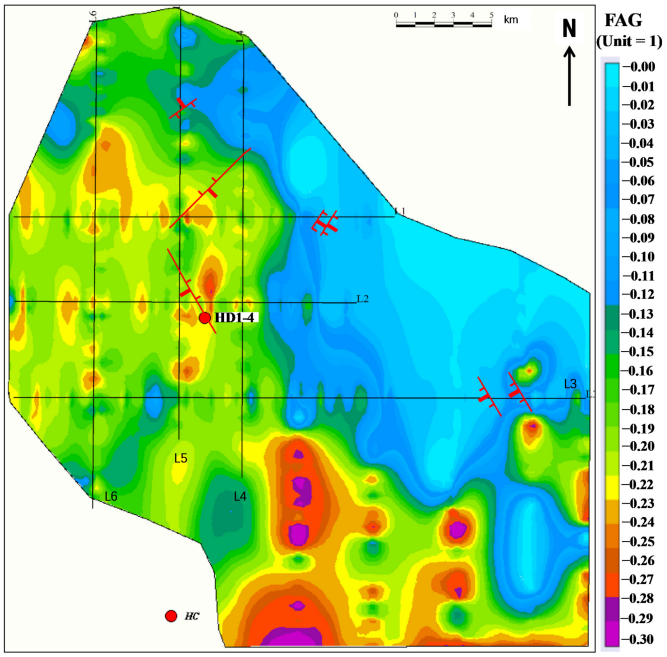


Figure 7. Deep karst prediction distribution map of seismic wave frequency attenuation gradient (FAG) technology in Huanjiang sag (including fault interpretation). The large attenuation gradient indicates the fractures and caves, which are represented by red color in the map. Note: The plane locations of Figure 7 are shown in Figure 1B. HC = Hechi city.

6. Geochemical Characteristics of Fracture-Cavity Fillings

6.1. Age Determination Results of Cave Fillings

The earthy yellow fine-grained calcite grown on the cave wall was taken from the 421 m cave wall for Th-U dating. The results show that the age of the earthy yellow fine-grained calcite in the deep karst cave is 25.418 ± 3.1087 million years (Table 2). It reflects that some calcite (symbiotic with earthy yellow mud) in the cave grew in the late Quaternary Pleistocene, and also represents that there was a deep karst space at least 250,000 years ago.

Table 2. Th-U dating results of calcite fillings in karst caves.

Sample Number	^{238}U (ppb)	^{232}Th (ppt)	^{230}Th/^{232}Th (Atomic × 10^{-6})	δ^{234}U* (Measured)	^{230}Th/^{238}U (Activity)	^{230}Th Age (yr) (Uncorrected)	^{230}Th Age (yr) (Corrected)	$\delta^{234}U_{Initial}$** (Corrected)	^{230}Th Age (yr BP) *** (Corrected)
DY	17 ± 0	24,412 ± 491	13 ± 0	150 ± 6	1.1124 ± 0.0136	289,757 ± 17,907	252,486 ± 31,087	306 ± 29	252,418 ± 31,087

$\delta^{234}U^*$ = ([^{234}U/^{238}U]*A*ctivity − 1) × *1000.* $\delta^{234}U_{initial}$** was calculated based on ^{230}Th age (T), i.e., $\delta^{234}U_{initial} = \delta^{234}U$measured × $e^{\lambda 234 \times T}$. ***B.P. stands for "Before Present" where the "Present" is defined as the year 1950 A.D.*

6.2. Characteristics of Rare Earth Elements of Mud Fillings in the Deep Karst Caves

Samples of mud filled from fractures and caves at different depths in Well HD1–4 were collected to carry out rare earth tests and analyses, including yellow mud filled with soil from the 47 m fracture (Figure 4a), yellow mud filled with soil from the 429 m cave, and brick-red calcareous mudstone from the 1220.4 m fracture (Figure 4e). The rare earth element standardization of sedimentary rocks usually uses North American shale (NASC) or post Archean shale (PAAS) as the standard value [41]. In this paper, the NASC standard value remeasured by Gromet et al. [42] is used for standardization. The test results were standardized with North American shale to form a rare earth distribution pattern (Figure 8). It was found that the REE distribution curves of mud filled in 47 m cracks and mud filled in 429 m caves had a good similarity and affinity, both showing that light rare earth was slightly lower than heavy rare earth, and Ce was negative. The REE distribution curves of calcareous clays filled in 1220.4 m cracks are different from those of the above two types of mud fillings in the karst caves. The light and heavy rare earth elements are depleted, but the curves are relatively flat. They have poor affinity.

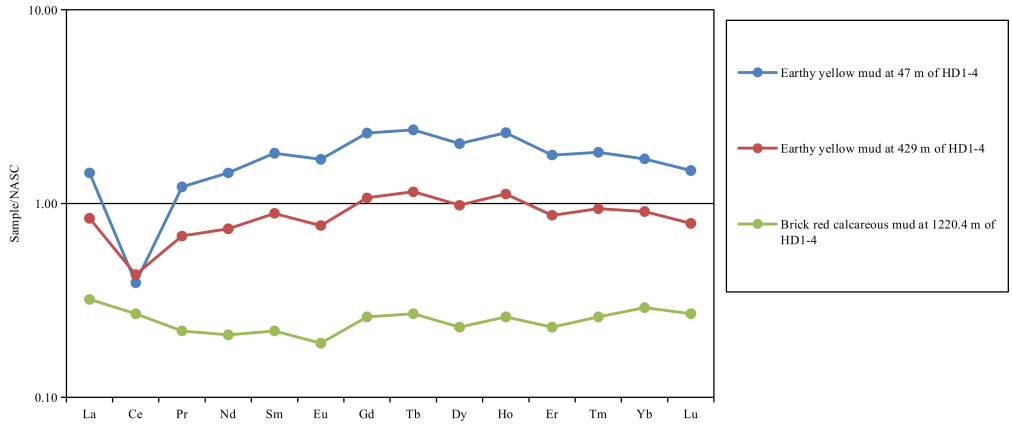


Figure 8. REE distribution pattern of mud filled at different depths of HD1-4. NASC = The REE value of North American shale as the standard value; REE = Rare earth elements.

6.3. Inclusion Characteristics of Chemical Deposits

Thirteen chemical deposits samples from the HD1-4 Well were selected, of which three samples were located in well section 415–484 m, and the other ten samples were located at depths of 1088 m and below, with the deepest being 1840 m. The homogenization temperature and freezing point temperatures of gas–liquid two-phase inclusions were tested by selecting calcite and dolomite in cracks and dissolved pores. A total of 107 gas–liquid two-phase fluid inclusions were tested. The test results are shown in Supplementary Material Table S1.

The temperature measurement results of gas–liquid two-phase inclusions show that the lowest homogenization temperature was 93 °C, and the highest was 225 °C. The low temperature inclusions below 90 °C are not detected, but there are a large number of single-phase inclusions in some calcites, and there is a room temperature to form calcite inclusions. According to the homogenization temperature distribution range of the inclusions (Figure 9), the inclusions were mainly distributed in two temperature ranges, of 100–120 °C and greater than 150 °C, of which 44 samples were in the range 100–120 °C and 41 samples were in the range greater than 150 °C, indicating that the inclusions are mainly formed in these two temperature ranges. According to the inclusion salinity (wt.% NaCl) calculated by freezing point temperature (Supplementary Material Table S1), 0.35% of low salinity inclusions and 14.57% of high salinity inclusions exist in deep karst space, reflecting the infiltration of low salinity fresh water in the deep karst space and the existence of high salinity formation water under closed burial conditions.

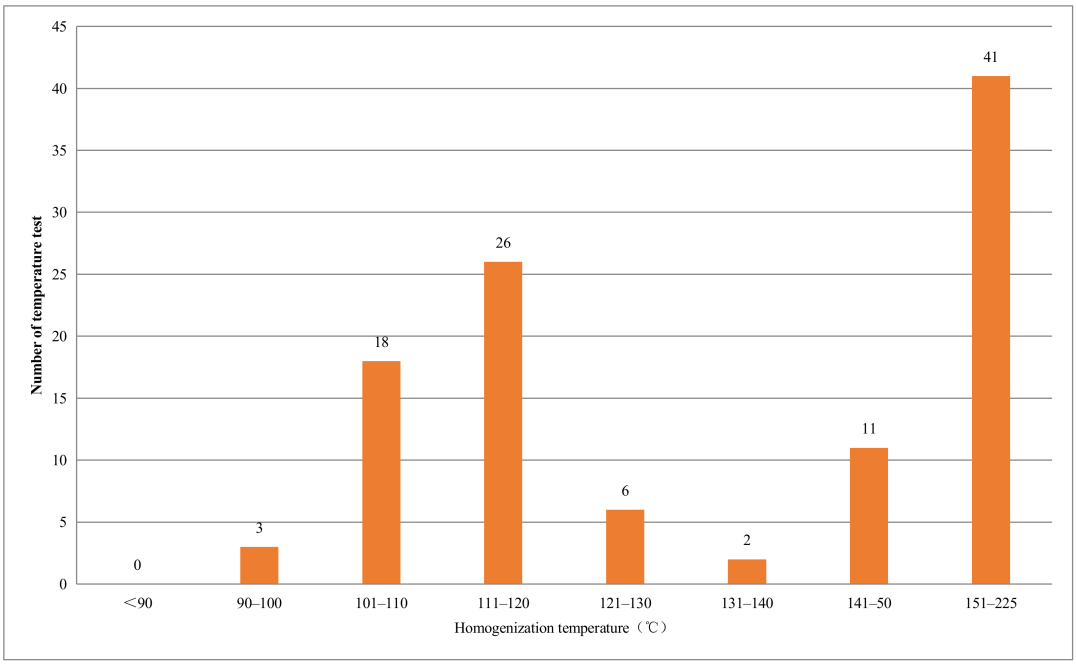


Figure 9. Temperature distribution range of chemical fillings in deep fracture-cavity of Huanjiang Sag.

7. Discussion

7.1. A Fault Is the Channel for Fluid Movement in Deep Karst and Control the Development of Deep Karst

A large number of network fractures, together with rock brecciation, porphyritic dissolution and the development of three sets of 6 m-thick calcite veins in the core (Figure 5), combined with the fact that Dong et al. [16] also found fault scratches and fault gravel on the surface outcrop near the well, prove that the deep karst space in this area is controlled by faults. In addition, the fault was traced in the seismic profile (Figure 6), and through multiple 2D seismic interpretations and a surface geological survey (Figure 7), it was found that the fault plane spreads in the NW direction and that the fault is of the compression type. Therefore, it is reasonable to speculate that the large calcite development section of the core is the core of the reverse fault (1400~1800 m), the upper part is the hanging wall of the fault, and the deep karst is developed in the hanging wall of the extrusion fault. The rock in the hanging wall of the fault is tensile as a whole, so tensile fractures are developed and along the tensile cracks, flesh shapes, plaque shapes and breccia shapes are formed. The development of large caves is related to regional groundwater movement, which is discussed in the following sections. According to results from the wide-field electromagnetic method and core observation, it was found that the deep karst space, with a width of up to 500 m and a depth of up to 1500 m (Figure 6), is linearly distributed along faults in the plane (Figure 10). Following investigation and staging of faults in this area according to a regional geological survey [30,31], the NW-striking faults should have been formed in the Yanshanian period. In summary , the hangingwall of the reverse fault is of a tensile nature, and tensile fractures are developed in the rock, which form the channels of deep karst fluid movement. Thick dolomite and limestone are developed in the hanging wall, and rich dissolution morphologies are formed in different rock types (Figures 3 and 4).

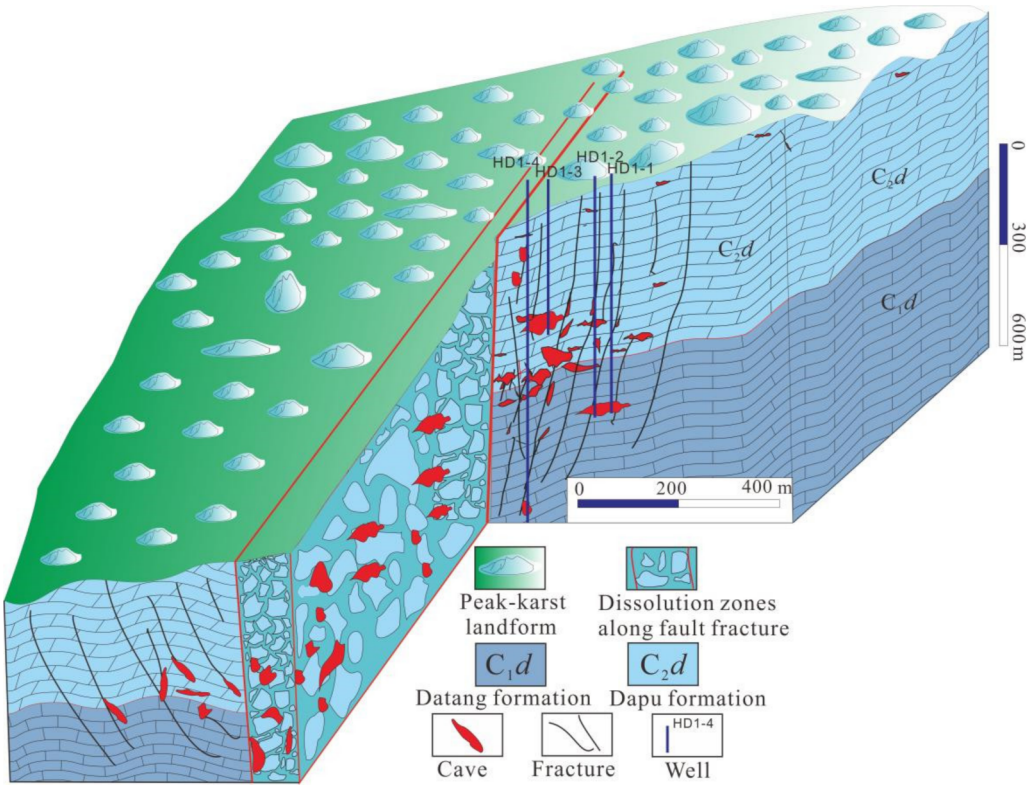


Figure 10. Distribution pattern of deep karst fracture-cavities controlled by a reverse fault in Huanjiang Sag. The width and height of karst voids was identified by the wide-field electromagnetic method (Figure 6).

7.2. Deep Karst Stages and Genetic Types

According to the analysis of karst spatial filling, the deep karst around Huanjiang is the product of multi-stage fluid action. There are at least two periods of obvious karstification.

7.2.1. Deep Hydrothermal Karst in Yanshanian Period

According to the burial history–thermal history analysis of the Guizhong 1 Well in the Huanjiang area by Pan et al. [43] (Supplementary Material Figure S3), the highest burial temperature of Carboniferous strata is between 150–160 °C. However, the temperature measurement of calcite inclusions filled with fractures and caves showed more inclusions greater than 150 °C, even up to 220 °C (Figure 9), which was greater than the maximum buried depth of the strata, indicating that there was underlying hydrothermal fluid mixed into the strata. From the regional geological map (Figure 1), the intrusive rock can be seen 50 km west of the drilling, which represents a regional thermal event. Wang et al. [44] used Ar^{40}/Ar^{39} dating of intrusive rocks and found that the intrusive rocks were formed in the Yanshanian Cretaceous at 90–100 Ma. Since no new intrusive rock has been found since the Yanshanian period in the study area, it is speculated that this set of intrusive rocks contains high temperature fluid, which leads to a high temperature in calcite inclusions filled in the fracture-cavity. According to the fault combination and cutting relationship, following the regional geological record [27,28] it is believed that the formation period of NW-trending faults passing through the well coincides with the Yanshanian period. Therefore, it is reasonable to speculate that the Carboniferous carbonate rocks were buried underground for a long time after deposition, until the Yanshanian tectonic activity formed faults, accompanied by magmatic intrusion (Figure 11). The underground high temperature fluid brought by magma entered the Carboniferous carbonate rocks along the fault and mixed with formation water. The mixing of fluids of different temperatures and salinities

increases the solubility of CO_2 and increases the solubility of the fluid [45], resulting in hydrothermal mixed karstification.

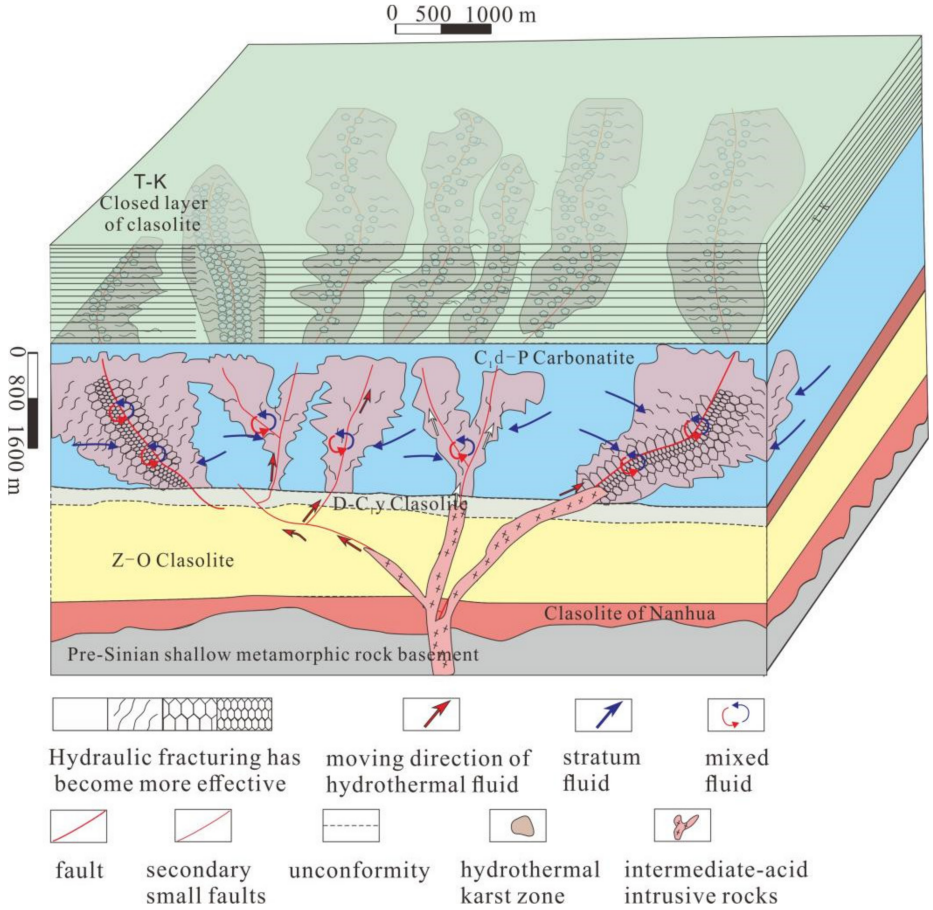


Figure 11. Fault and magmatic hydrothermal activity induced by Yanshanian tectonic activity in Huanjiang Sag.

7.2.2. Meteoric Water Deep Circulation Karst after the Himalayan Period

A large amount of earth-yellow mud and brick-red calcite was found in the fillings of the deep karst space (Figure 4), which reflects that the deep karst space is now open and affected by surface oxidation. Firstly, the rare earth element analysis shows that the mud filled in the 429 m cave has good affinity with the mud filled in the 47 m cave (Figure 8), which reflects that they are all derived from the overlying surface environment. Both of them also show negative Ce anomalies, which may be due to the oxidation of Ce^{3+} to Ce^{4+} in the mud under the surface environment, resulting in the remaining Ce^{4+} on the surface, which is difficult to migrate and thus enriched, while the mud infiltrated into the underground space shows Ce loss. The brick-red calcareous mud filled in the 1220.4 m crack is actually the original broken rock, infected by purple-red Fe, and mixed with calcite. Therefore, it is not consistent with the rare earth distribution curve of cave argillaceous fillings, but the occurrence of brick-red calcite shows that the influence of the surface oxidation environment is weakened at this depth. Next, very low salinity inclusions (wt.% NaCl = 0.35%) were also found in deep karst space (Supplementary Material Table S1), which confirms that meteoric water penetrated into the deep underground space. With the infiltration of mud, earth-yellow calcite grows in the caves of the 421 m section, which was proven to have formed in Quaternary by dating results (Table 2). In addition, the analysis of groundwater sampling in karst caves from Dong et al. [16] also found that the mineralization degree of groundwater in deep karst caves was not high, and an isotope analysis showed that the groundwater in karst caves was homologous to the southern spring Hs010, indicating

that the formation of deep karst caves was affected by the deep circulation karstification of meteoric water (Figures 2 and 12).

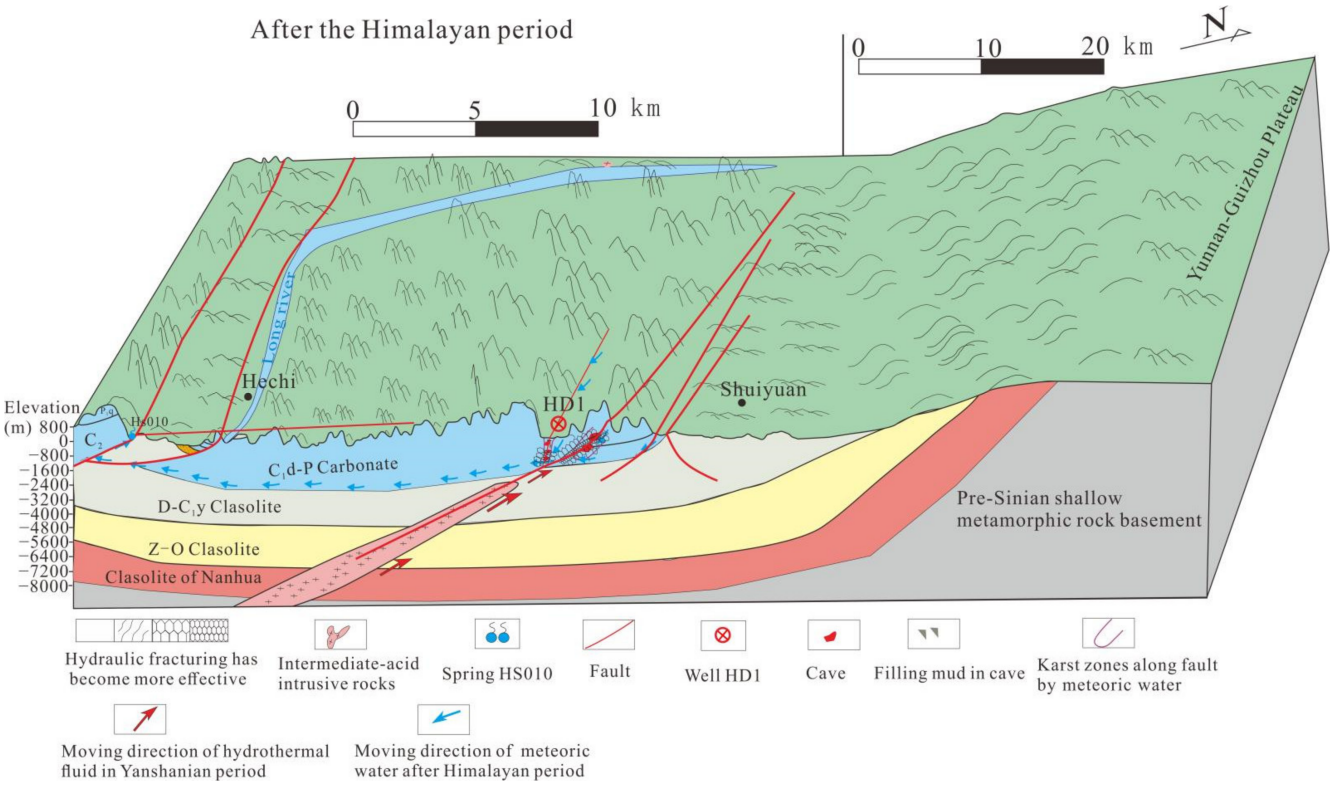


Figure 12. Meteoric water deep circulation karst after the Himalayan period in Huanjiang Sag. The Yunnan-Guizhou Plateau was uplifted after the Himalayan period, and the strata denudation caused the fault to open to earth. A deep karst space developed again along the fault through meteoric fresh water. The dissolution characteristics of the fault zone are shown in Figure 10.

The deep circulation time of meteoric water should be later than the opening time of the deep cave. According to deep cave dating, the action time of meteoric water should be more than 250,000 years. Following analysis from regional tectonic evolution [29,46], the Huanjiang sag is located in the southern slope of the Yunnan-Guizhou Plateau. New research shows that the high elevation of the Yunnan-Guizhou Plateau had developed before the Late Pliocene (3.54 Ma) [47], thus, its Himalayan orogeny is the main reason for the exposure of the Carboniferous strata to the surface and the acceptance of meteoric water karst in this area, which is also in line with the dating results. As for whether there is hydrothermal karst in the deep circulation karst process of groundwater after the Himalayan period, we believe that the age of the cave infilling is too distant from the intrusions to provide the heat for the fluids, and that therefore the two karst types did not develop together in the same period.

7.3. Evolution of Deep Karst of Different Genetic Types

The formation of deep karst around Huanjiang is due to the comprehensive effects of Yanshanian hypogene hydrothermal karst and post Himalayan meteoric water deep circulation karst (Figures 11 and 12). The basic conditions of deep karst development are thick carbonate rocks of Carboniferous and developed faults, and further, the fluid activities in different periods lead to the inherited development of deep karst.

After the Carboniferous strata were deposited, they were buried deep underground (Supplementary Material Figure S3). It was not until the tectonic activities in the Yanshanian period that regional magma intrusion led to deep hydrothermal activity along the

penetrating carbonate faults. It is reasonable to speculate that the deep karst space was initially dissolved (Figure 11). The continuous tectonic uplift in the Himalayan period led to the direct exposure of Carboniferous strata in this area to the surface [46]. We speculate that the faults were open to the earth and meteoric water infiltrated, leading to the evolution of deep karstification types (Figure 12). The final formation of the large karst space in Well HD1, the filling of mudstone in the karst cave and the transformation of white calcite to brick-red calcite are related to the transformation of deep karst mechanisms from deep hydrothermal karst to meteoric water deep circulation karst. The topographic difference caused by the uplift of the Yunnan-Guizhou Plateau is high in the north and low in the south, and Dong et al. [16] claimed that there is a head difference between the north and the south of the Huanjiang sag structure (Figure 2), which ensures the dynamic energy of deep groundwater circulation. From the karst results, it is obvious that the open groundwater deep circulation karstification has stronger dissolution compared to the hydrothermal karst in the Huanjiang area.

8. Conclusions

The deep karst in Huanjiang area is mainly composed of net cracks, holes expanding along cracks and dolomite honeycomb pores, and large karst caves are also developed, which are related to NW-trending compression faults. The deep karst space is developed in the hanging wall of the fault, with a width of 500 m and a height of 1500 m, and linear distribution along NW faults in the region. The development of deep karst space is related to two deep karst genetic types: The first is the hypogene hydrothermal karst, which developed in the Yanshanian period and is related to regional magmatism. The second is the groundwater deep circulation karst, mainly developed after the Himalayan period, which is related to the deep circulation of meteoric water. The genesis of the deep karst space is the result of multi-stage karst superposition and is mainly controlled by faults. It is difficult to determine the specific time points of these two types of deep karst transformation, but according to regional tectonic evolution, we speculate that the Yunnan-Guizhou Plateau has been uplifted since the Himalayan period (3.54 Ma), and the Carboniferous carbonate rocks and early faults in the Huanjiang area have been exposed, leading to the change and evolution of deep karst. Through comprehensive analysis, a fault-controlled hypogene hydrothermal karst pattern and a meteoric water deep karst pattern were established. The above research results have special significance for understanding the process and genetic mechanism of deep karst in other regions of the world, and are of great significance for enriching karst geological theory. The genetic pattern of deep karst provides theoretical support for predicting this kind of karst in southern China and avoiding drilling deep karst caves in the course of resource development.

Supplementary Materials: The following supporting information can be downloaded at: https://www.mdpi.com/article/10.3390/min12040405/s1, Figure S1: Karst landform and four wells' position near Well HD1 in Huanjiang Sag; Figure S2: Characteristics of dissolved pores and caves in deep karst space of HD 1; Figure S3: Burial history-thermal history map of Well Guizhong 1 in Huanjiang Sag; Figure S4: L1 2D Seismic Geological Interpretation and Uninterpretation Sections; Figure S5: L2 2D Seismic Geological Interpretation and Uninterpretation Sections; Figure S6: L3 2D Seismic Geological Interpretation and Uninterpretation Sections; Figure S7: L4 2D Seismic Geological Interpretation and Uninterpretation Sections; Figure S8: L5 2D Seismic Geological Interpretation and Uninterpretation Sections; Figure S9: L6 2D Seismic Geological Interpretation and Uninterpretation Sections; Table S1: Test results of gas-liquid two-phase inclusion of chemical deposits in deep caves and cracks of Huanjiang Sag.

Author Contributions: Conceptualization, Y.D.; methodology, Y.D.; formal analysis, Y.D.; investigation, G.N., K.H., X.H. and S.J.; writing—original draft preparation, H.D.; writing—review and editing, Y.D.; project administration, B.L. and Y.D.; all the co-authors performed a critical revision of the intellectual content of the paper. All authors have read and agreed to the published version of the manuscript.

Funding: This research was funded by the Natural Science Foundation of Guangxi, China (2020GXNSFAA297095, 2021AB29005, 2020AB22013), the National Key R&D Program of China (No. 2018YFC0604301, 41902261), the Nonprofit Industry Research Program of the Chinese Academy of Geological Sciences (YYWF201723), the Geological Survey Program of the China Geological Survey (DD20190723, DD20221658), the basic research program of the Institute of Karst Geology, Chinese Academy of Geological Sciences (2020012, 2020018).

Institutional Review Board Statement: Not applicable for studies not involving humans or animals.

Informed Consent Statement: Not applicable for studies not involving humans.

Data Availability Statement: Compliance with MDPI Research Data Policies.

Acknowledgments: Shi Di-Shi of the Center of Oil and Natural Gas Resource Exploration, China Geological Survey, was of great assistance during core observation and two-dimensional seismic data collection. Du Wen-Yue and Yang Hui of the Institute of Karst Geology of the Chinese Academy of Geological Sciences were of great support during sample testing and analysis processes. Yin Jian-Jun of the Institute of Karst Geology of the Chinese Academy of Geological Sciences were of great support during U-Th dating.

Conflicts of Interest: The authors declare no conflict of interest.

References

1. Palmer, A.N. Origin and morphology of limestone caves. *Geol. Soc. Am. Bull.* **1991**, *103*, 1–21. [CrossRef]
2. Kunsky, J. Thermomineral karst and caves of Zbrasov, Northern Moravia. *Proc. Czechoslov. Soc. Geol.* **1957**, *62*, 306–351.
3. Dublyansky, Y.N. Hydrothermal karst in the Alpine folded region of the South of the USSR. *Kras I Speleol.* **1980**, *3*, 18–36.
4. Dublyansky, Y.V. Speleogenetic History of the Hungarian Hydrothermal Karst. *Environ. Geol.* **1995**, *25*, 24–35. [CrossRef]
5. Dublyansky, Y.V. *Speleogenesis: Evolution of Karst Aquifers*; National Speleological Society: Huntsville, AL, USA, 2000; pp. 298–303.
6. Ford, D.C.; Williams, P.W. *Karst Geomorphology and Hydrology*; Unwin Hyman: London, UK, 1989; p. 601.
7. Ford, D.C. Karst geomorphology, caves and cave deposits: A review of North American contributions during the past half century. In *Perspectives on Karst Geomorphology, Hydrology and Geochemistry*; Paper, 404; Harmon, R.S., Wicks, C.W., Eds.; GSA Special: Boulder, CO, USA, 2006; pp. 1–14.
8. Egemeier, S.J. Cavern development by thermal waters. *Natl. Speleol. Soc. Bull.* **1981**, *49*, 31–51.
9. Hill, C.A. *Geology of Carlsbad Cavern and other Caves in the Guadalupe Mountains, New Mexico and Texas*; New Mexico Bureau of Mines & Mineral Resources: Socorro, NM, USA, 1987; Volume 117, p. 150.
10. Klimchouk, A.B. *Hypogene Speleogenesis: Hydrogeological and Morphogenetic Perspective*; Special Paper 1; National Cave and Karst Research Institute: Carlsbad, NM, USA, 2007; p. 106.
11. Palmer, A.N. *Cave Geology*; Cave Books: Dayton, OH, USA, 2007.
12. Anette, S.E.; Libby, A.S. Microbial contributions to cave formation: New insights into sulfuric acid speleogenesis. *Geology* **2004**, *32*, 369–372.
13. Audra, P.; D'antoni-Nobecourt, J.C. Hypogenic caves in France. Speleogenesis and morphology of the cave systems. *Bull. Soc. Geol. Fr.* **2010**, *181*, 327–335. [CrossRef]
14. Walker, J.; Almasi, I.; Potma, K.; O'Keefe, J. Hypogenic karst beneath the Athabasca Oil Sands: Implications for oil sands mining operations. *Bull. Can. Petrol. Geol.* **2017**, *65*, 115–146. [CrossRef]
15. Frumkin, A.; Langford, B.; Lisker, S.; Amrani, A. Hypogenic karst at the Arabian platform margins: Implications for far-field groundwater systems. *Bull. Geol. Soc. Am.* **2017**, *129*, 1636–1659. [CrossRef]
16. Dong, H.Q.; Dan, Y.; Liang, J.P.; Liang, B.; Nie, G.Q.; Ji, S.C. A Hypogene Karst Development Pattern Controlled by the Deep-Cycle of Groundwater in the Syncline in Huanjiang, Guangxi, China. *Water* **2021**, *13*, 199. [CrossRef]
17. Li, M.Q. The Simulation Study Deep karst Formation Conditions. In *Karat Caves and Physiognomy*; Science Press: Beijing, China, 1985. (In Chinese)
18. Zou, C.J. Application of tritium analysis to the study of deep karst and seepage problems at reservoir and dam sites. *Carsol. Sin.* **1988**, *7*, 132–138. (In Chinese)
19. Li, Y.C.; Han, B.P. Deep karst periods and types in the Tengxian and Peixian coal bearing basin. *Procedia Earth Planet. Sci.* **1993**, *11*, 59–61. (In Chinese)
20. Huang, S.Y.; Song, H.R. Deep karstification of gas-oil reservoir. *Carsol. Sin.* **1997**, *16*, 189–198. (In Chinese)
21. Xia, R.Y. New progress in the study of paleokarst and deep karst in oil and gas fields. *Carsol. Sin.* **2001**, *20*, 76. (In Chinese)
22. Xu, M.; Mao, B.Y.; Zhang, Q. Evolvement and ecpectation of research on the modern deep karst. *Adv. Earth Sci.* **2008**, *23*, 495–501. (In Chinese)
23. Sauro, F.; Zampieri, D.; Filipponi, M. Development of a deep karst system within a transpressional structure of the dolomites in north-east italy. *Geomorphology* **2013**, *184*, 51–63. [CrossRef]

24. Mao, B.Y.; Xu, M.; Bai, A.Z. Study on the Karst Development Law and Mechanism of Heshan Coal Field in Guangxi Province. *Res. Soil Water Conserv.* **2008**, *1*, 205–208. (In Chinese)
25. Pan, W.Q.; Liu, Y.Y.F.; Dickson, J.A.D.; Shen, A.J.; Han, J.; Ye, Y.; Gao, H.L.; Guan, P.; Zheng, X.P. The Geological Model of Hydrothermal Activity in Outcrop and the Characteristics of Carbonate Hydrothermal Karst of Lower Paleozoic in Tarim Basin. *Acta Sedimentol. Sin.* **2009**, *27*, 983–994. (In Chinese)
26. Frumkin, M. Deep confined karst detection, analysis and paleo-hydrology reconstruction at a basin-wide scale using new geophysical interpretation of borehole logs. *J. Hydrol.* **2011**, *406*, 158–169.
27. Regional Geological Survey Report of Luocheng Sheet (scale, 1:200,000). In *The Geological Survey of Guangxi Zhuang Autonomous Region*; Guangxi Geological Bureau Press: Nanning, China, 1968. (In Chinese)
28. Regional Geological Survey Report of Donglan Sheet (scale, 1:200,000). In *The Geological Survey of Guangxi Zhuang Autonomous Region*; Guangxi Geological Bureau Press: Nanning, China, 1971. (In Chinese)
29. Wu, G.; Yao, G.; Xu, Z.; Guo, Q.; Chen, Z. Structural patterns and origin of tectonic reformation in guizhong depression. *Mar. Orig. Pet. Geol.* **2009**, *14*, 33–40. (In Chinese)
30. Liu, B.; Li, S.Z.; Zhou, Y.G.; Jin, C.; Dai, L.M.; Liu, L.P.; Wang, T.; Wang, J.; Hao, Y.; Liu, E.S. Structural features and evolution of the Hechi-Yizhou fault zone, northern Guangxi-insights from shallow to deep structures of its Liucheng segment. *Geotecton. Metallog.* **2009**, *33*, 488–496. (In Chinese)
31. Mao, P.X.; Jin, A.M.; Lou, Z.H. Investigation of pore structure and fractal characteristics of marine shale reservoirs of the Upper Paleozoic in Huanjiang sag, Guizhong depression. *Chin. J. Geol.* **2019**, *54*, 130–144. (In Chinese)
32. Klimchouk, A.; Auler, A.S.; Bezerra, F.; Cazarin, C.L.; Balsamo, F.; Dublyansky, Y. Hypogenic origin, geologic controls and functional organization of a giant cave system in precambrian carbonates, brazil. *Geomorphology* **2016**, *253*, 385–405. [CrossRef]
33. Bögli, A. *Karst Hydrology and Physical Speleology*; Springer: Berlin, Germany, 1980.
34. Dan, Y.; Lin, L.; Liang, B.; Zhang, Q.; Yu, Y.; Cao, J. Eogenetic karst control of carbonate reservoirs during a transient exposure: A case study of the ordovician yingshan formation in the northern slope of the tazhong uplift, tarim basin, China. *Minerals* **2018**, *8*, 345. [CrossRef]
35. Zhang, J.; He, Z.H.; Huang, D.J. Application of frequency attenuation gradient in prediction of gas and oil potentials. *Prog. Explor. Geophys.* **2010**, *33*, 207–211.
36. Huafeng, H.U.; Bao, D.; Lingwei, M.A.; Qi, H.U. Scale characterization of carbonate karst cave reservoirs based on high-frequency attenuation gradient: A case study from karst paleochannels reservoirs in tahe oilfield, China. *Geophys. Prospect. Pet.* **2018**, *57*, 892–900. (In Chinese)
37. Yuan, B.; Li, D.; Bayless, R.C. Wide field electromagnetic method for shale gas exploration in southern china: A case study. *J. Environ. Eng. Geophys.* **2017**, *22*, 279–289. [CrossRef]
38. Shen, C.C.; Edwards, R.L.; Cheng, H.; Dorale, J.A.; Edmonds, H.N. Uranium and thorium isotopic and concentration measurements by magnetic sector inductively coupled plasma mass spectrometry. *Chem. Geol.* **2002**, *185*, 165–178. [CrossRef]
39. Cheng, H.; Edwards, R.L.; Shen, C.-C.; Woodhead, J.; Hellstrom, J.; Wang, Y.J.; Kong, X.G.; Spötl, C.; Wang, X.F.; Alexander, E.C., Jr. Improvements in 230 Th dating, 230 Th and 234 U half-life values, and U-Th isotopic measurements by multi-collector inductively coupled plasma mass spectrometry. *Earth Planet. Sci. Lett.* **2013**, *371–372*, 82–91. [CrossRef]
40. Nothdurft, L.D.; Webb, G.E.; Kamber, B.S. Rare earth element geochemistry of Late Devonian reefal carbonates, Canning Basin, Western Australia: Confirmation of seawater REE proxy in ancient limestones. *Geochim. Cosmochim. Acta* **2004**, *68*, 263–283. [CrossRef]
41. Yi, H.S.; Lin, J.H.; Zhao, X.X. Geochemistry of Rare Earth Elements and Origin of Positive Europium Anomaly in Miocene-Oligocene Lacustrine Carbonates from Tuotuohe Basin of Tibetan Plateau. *Acta Sendimentologica Sin.* **2008**, *26*, 1–10.
42. Gromet, L.P.; Haskin, L.A.; Korotev, R.L. The "North American Shale Composite": Its Compilation, Major and Trace Element Characteristics. *Geochim. Coamochimica Acta* **1984**, *48*, 2469–2482. [CrossRef]
43. Pan, R.; Tang, X.; Meng, J. Shale gas preservation conditions for the Upper Paleozoic in Guizhong Depression. *Oil Gas Geol.* **2014**, *35*, 534–541.
44. Wang, D.; Chen, Y.; Chen, W.; Sang, H.; Lin, Z. Dating the dachang giant tin-polymetal lic deposit in nandan, guangxi. *Acta Geol. Sin.* **2004**, *78*, 133–138.
45. Bögli, A. Mischungkorrosion; ein Beitrag zum Ver karst ungs problem. *Erdkunde* **1964**, *18*, 83–92. [CrossRef]
46. Wei, Y.; Chengzhan, L.I.; Chen, W.; Luo, Q.; Zhu, D.; Pan, T. Characteristics and formation and evolution analysis of the karst landscape of guangxi. *Guangxi Sci.* **2018**, *25*, 465–504.
47. Yu, L.; Shijie, W.; Sheng, X.; Derek, F.; Finlay, M.S.; Ángel, R.; Xinbao, Z.; Weijun, L. New chronological constraints on the Plio-Pleistocene uplift of the Guizhou Plateau, SE margin of the Tibetan Plateau. *Quat. Geochronol.* **2022**, *67*, 101237.